Microstructural and Mechanical Evolution of a Low Carbon Steel by Friction Stir Processing

DURSUN MURAT SEKBAN, SEMIH MAHMUT AKTARER, HAO ZHANG, PENG XUE, ZONGYI MA, and GENCAGA PURCEK

A low carbon steel (Grade A) was subjected to friction stir processing (FSP), and the effect of FSP on the microstructure and mechanical properties was investigated systematically. It was found that two distinct zones called stir zone (SZ) and heat-effected zone (HAZ) were formed during FSP. The SZ and HAZ consist mainly of ferrite, widmanstatten ferrite, ferrite + cementite aggregates, and martensite. FSP considerably refined the microstructure of the steel by means of dynamic recrystallization mechanism and formed a volumetric defect-free basin-like processed region. The ferritic grain size of the steel decreased from 25 μm in the coarse-grained state to about 3 μm in the fine-grained state, and the grains formed were separated mostly by high angle of misorientation with low density of dislocations. This microstructural evolution brought about a considerable increase in both hardness and strength values without a considerable decrease in ductility. Ultrafine-grained microstructure formed around and just beneath the pin increased the hardness of the steel from 140 Hv0.3 to about 245 Hv0.3. However, no hardness uniformity was formed throughout the processed zone due to the changes in deformation- and temperature-induced microstructure. Both yield and tensile strength values of processed zone increased from 256 and 435 MPa to about 334 and 525 MPa, respectively.

DOI: 10.1007/s11661-017-4157-z

I. INTRODUCTION

PLAIN or low carbon steels have gained a great interest in many industries like ship building, automotive construction, and oil and gas operational systems because of low cost and high performance such as good toughness, high corrosion resistance, and good welding properties.[1] However, their mechanical properties such as strength, hardness, and fatigue resistance are relatively low due to their low carbon content in annealed conditions. The main advantage of such steel is that their microstructural and mechanical properties can easily be improved by heat treatment, plastic deformation, and grain refinement techniques without alloying or changing their chemical compositions. Among them, microstructural modification by grain refinement is becoming one of the main essential strengthening mechanisms due to the recently developed novel processing techniques that are capable of enhancing strength and fatigue resistance of metallic materials with adequate toughness behavior.[2]

Many viable grain refinement techniques have been proposed so far. The techniques based on severe plastic deformation (SPD) seem to be the most suitable ones because of their high capability of grain refinement.[3,4] Among SPD methods, equal-channel angular extrusion/pressing (ECAE/P), high pressure torsion (HPT), accumulative roll bonding (ARB), and friction stir processing (FSP) are well known ones.[5] The FSP is the best one among others considering the processing of large-scale plate or sheet type of materials.[6]

Regarding FSP, many regular and review papers have been published till now, and more detailed information can be obtained in literature.[7–10] Shortly, FSP is a novel microstructural modification technique developed based on the principles of friction stir welding (FSW) method.[11] In FSP, a non-consumable rotating tool with a shoulder and pin is inserted into a metal plate or sheet and traverses through a direction of interest. The heat generated by friction between rotating tool and metal surface locally softens the volume to be processed. The stir zone (SZ) is constituted generally by

DURSUN MURAT SEKBAN is with the Department of Naval Architecture and Marine Engineering, Karadeniz Technical University, 61080 Trabzon, Turkey. SEMIH MAHMUT AKTARER is with the Department of Automotive Technology, Recep Tayyip Erdogan University, 53020 Rize, Turkey. HAO ZHANG, PENG XUE and ZONGYI MA are with the Shenyang National Laboratory for Materials Science, Institute of Metal Research, Chinese Academy of Sciences, Shenyang 110000, China. GENCAGA PURCEK is with the Department of Mechanical Engineering, Karadeniz Technical University, 61080 Trabzon, Turkey, and also with the Engineering Faculty, Giresun University, Giresun, Turkey. Contact e-mail: purcek@ktu.edu.tr

Manuscript submitted January 11, 2017.
Article published online May 30, 2017

dynamically recrystallized (DRX) fine grains due to localized SPD.[7] As a result of grain refinement by FSP, the properties of metallic materials such as strength, fatigue, and wear resistance can be improved considerably by applying suitable processing parameters.[12]

By looking at the application of FSP to the steels, it can be said that many types of steels/plates have been processed so far. Among them, ultra-low carbon steels (or IF steel),[13,14] low carbon steels,[2] medium carbon steels,[15] high carbon steels,[16–19] high strength low alloy (HSLA) steels,[20,21] tool steels,[12,22–24] dual-phase (DP) steels,[25] structural steels,[26,27] Co-Cr-Fe alloys,[28] hydro-turbine steels,[29,30] ODS ferritic steels,[31] and stainless steels[32–36] have been investigated. However, few studies have been conducted on FSP of low carbon steels. Xue *et al.*[2] reported that ultrafine dual-phase structure such as ferrite–martensite was successfully achieved in plain low carbon steel *via* FSP. They also showed that ultimate tensile strength of the parent materials increased dramatically from 520 MPa to about 1350 MPa. Sekban *et al.*[13] investigated the formability of FSPed IF steel as well as its microstructure and mechanical properties. They found that the formability and mechanical properties of FSPed IF steel improved considerably during FSP due to the substantial grain refinement. Another study on the formation of nano-grained IF steel after FSP was carried out by Chabok *et al.*[14] They reported that FSP resulted in the formation of a 30 to 35 μm thick surface layer with the grain size of 50 to 125 nm in that steel.

In view of the above, FSP has a growing interest among the scientists and technological implementers, and thus the gaps in literature should be filled by detailed studies especially on the processing–microstructure–mechanical property relationships. Considering the technological applications, low carbon or plain carbon steel plates or sheets have been used extensively in many technological applications. Although many studies have been performed on other types of steels, very limited works have been carried out on low carbon steel plates and sheets. Thus, it is necessary to identify the microstructural evolution during FSP of such steel plates in order to understand the relationship between processing–microstructure–mechanical properties better. Therefore, the main purpose of this study is to systematically investigate the microstructural characterization with quantitative/qualitative measurements of a low carbon steel after FSP, and to evaluate the effect of microstructural alteration on the main mechanical properties. Additionally, the effect of temperature on the microstructure in the FSPed zone was also employed to provide in-depth insight into microstructural evolution.

II. EXPERIMENTAL PROCEDURES

A low carbon steel (Grade A steel according to ASTM 131A) in the form of hot-rolled plates with a chemical composition of 0.16 wt pct C, 0.18 wt pct Si, 0.7 wt pct Mn, 0.11 wt pct S, 0.18 wt pct P, 0.09 wt pct Cr, 0.14 wt pct Mo, 0.04 wt pct Cu, 0.04 wt pct V, and balance Fe was utilized as the starting material. Samples for FSP with dimensions of 200 mm × 40 mm × 6 mm were machined from those plates. FSP was performed at a tool rotation of 630 rpm and a traverse speed of 45 mm min^{-1} using a processing tool which has a convex shoulder with the diameter of 18 mm and a cylindrical pin with the diameter and length of 8 and 3 mm, respectively. The shoulder tilt angle was set at 3^0, and tool plunger downforce was 11 kN during the process.

The microstructural characterization of steel plates before and after FSP was characterized by optical microscope (OM), scanning electron microscope (SEM), and transmission electron microscope (TEM). Samples for OM and SEM investigations were sectioned perpendicular to the process direction (Figure 1(a)) and then etched with 3 pct Nital for 15 s after standard metallographic preparation. SEM was used in the secondary electron imaging mode at the voltage of 15 keV. For TEM investigations, the specimens were mechanically ground and polished down to 0.15 mm thick foils. Large electron-transparent areas were obtained by subsequent ion milling with a ±4.5 deg inclination angle of the beam on both sides of the specimen with 5.5 keV and 30 μA ion current. Subsequently, the milling-affected surface layer was removed with a 1 keV and 5 μA ion beam. TEM investigations were carried out using a Philips CM-200 microscope operated at a nominal voltage of 200 kV.

Mechanical properties before and after FSP were determined using hardness and tensile tests. Hardness measurements were performed using a Vickers micro-hardness tester operated under a load of 300 g and a dwell time of 10 seconds. Hardness was scanned along the cross section of the processed sample (Figure 1). At least five measurements were taken for each point to see the repeatability of the results. Hardness measurements were also done step by step throughout the processed zone as shown in Figure 1, and a contour map representation was presented to show the uniformity in the distribution of hardness values throughout the FSPed zone. Dog-bone-shaped specimens with the gage sections of 2 mm × 3 mm × 13 mm were taken from the processed region for the tensile tests (Figure 1). The tensile axis of the specimen was oriented parallel to the processed direction of the FSPed plate. The tests were performed using an Instron-3382 electro-mechanical testing frame with a video-type extensometer at a quasi-static strain rate of 5.4 × 10^{-4} s^{-1}. At least, three tests were conducted, and the mean results of them were taken as the mean strength and ductility values.

III. RESULTS AND DISCUSSION

A. *Microstructure*

Optical micrographs showing the global microstructure of steel plates before FSP are shown in Figures 2(a) and (b). As seen clearly, they exhibit a typical structure for a plain low carbon steel with ferritic (white in color) and pearlitic (dark in color) phases. An elongated or

banded pearlitic phase coming from the hot rolling process is also seen through the microstructure (Figure 2(a)). The pearlitic phase is located mainly along the boundaries of ferritic grains. However, the ferritic phase consists mainly of equiaxed coarse grains with an average size of 25 μm due to recrystallization during initial hot rolling process (Figure 2(b)). In the as-received microstructure, the ratio of pearlitic phase was measured to be about 20 pct.

Optical and SEM micrographs showing the effect of single-pass FSP on the microstructure of steel plates are shown in Figure 3. In general, FSP leads to a significant refinement in the microstructure into the processed zone with predominant equilibrium grain boundaries. In the processed region, the coarse-grained (CG) structure of as-received steel transforms into the fine-grained (FG) structure after FSP. It can be stated that FSP brings about a microstructure similar to that obtained with the conventional welding of such steels (Figure 3(a)). Thus, the microstructure formed by FSP was classified according to a scheme developed by the International Institute for Welding (IIW).[37] So the processed region consists of two distinct zones: stir zone (SZ) and heat-affected zone (HAZ) (Figure 3(a)). The SZ exhibits a characteristic nature of dynamic recrystallization during processing.[7,11] This zone undergoes both intense plastic deformation and frictional heating during FSP and results in different microstructural features. Peak temperature in that zone was experimentally measured to be around 1103 K (930 °C) during processing, at which the Grade A steel was in the austenitic (Υ) phase region.

The microstructure of the SZ is characterized by equiaxed fine ferrite, grain boundary ferrite (PF (G)), aligned and non-aligned widmanstatten ferrite (WF-FS(A), FS(NA)), and aggregates of ferrite + cementite (FC) (Figures 3(b) through (g)). A thin layer of equiaxed FG microstructure named as "shoulder-affected SZ" with the thickness of about 200 μm is formed just under the shoulder (Figure 3(b)). The average size of ferrite grains in that zone is about 5 μm. Optical and SEM micrographs representing the microstructure in the middle of the SZ are shown in Figures 3(c) and (d), where the microstructures consist mainly of grain boundary ferrite, Widmanstatten ferrite, and aggregates of ferrite + cementite. In low carbon steels, the first phase usually forming prior austenite on the grain boundaries during cooling below the A_3 is known as allotriomorphic ferrite which is termed by PF(G) in (Figure 3(d).[38] As a classical feature, the formation of Widmanstatten ferrite may occur at relatively low cooling rate. These ferrite plates grow rapidly with a high aspect ratio (~10:1). Widmanstatten ferrite growing at grain boundary sites prior austenite is usually seen as colonies of aligned coarse plates which are termed as FS(A) in the IIW scheme[39] (Figure 3(c)).

A FG microstructure similar to the microstructure in Figure 3(b) is also formed just beneath the SZ (Figure 3(e)). Because that region just beneath the pin end undergoes an intense plastic deformation, the microstructure in that region exhibits fine ferrite grains

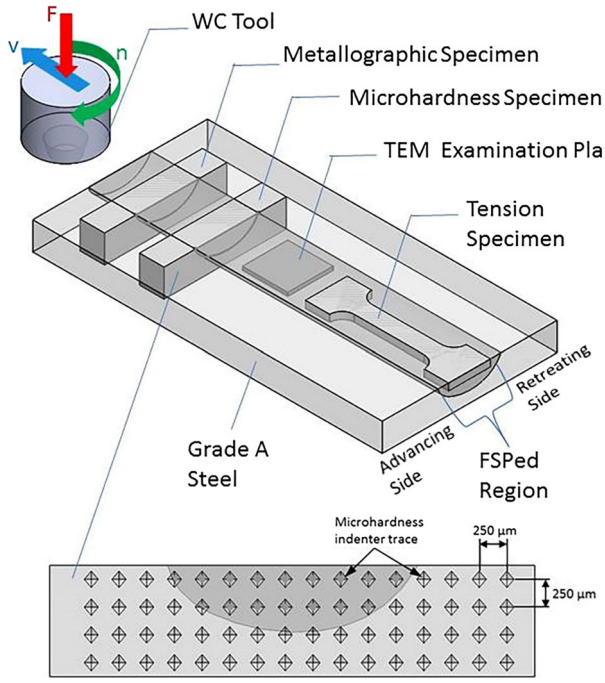

Fig. 1—Schematic illustrations of FSPed plate, and geometries and positions of the test specimens in that processed plate.

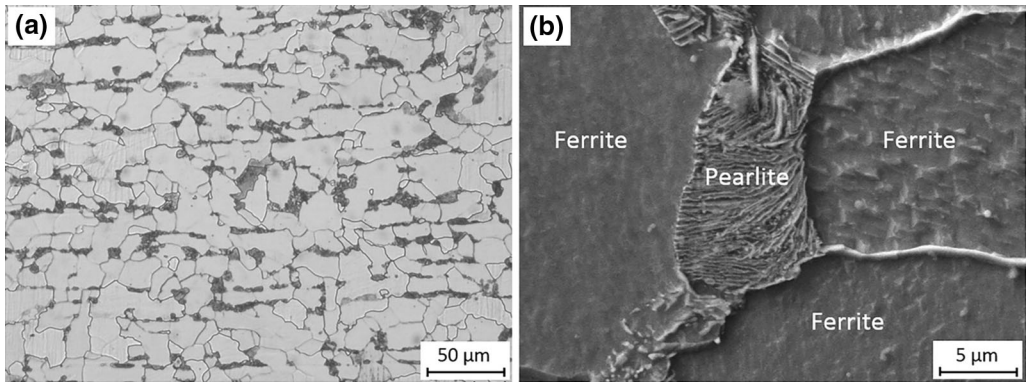

Fig. 2—Micrographs showing the microstructure of coarse-grained (CG) as-received steel plates: (*a*) Low magnification optical micrograph and (*b*) high magnification SEM micrograph.

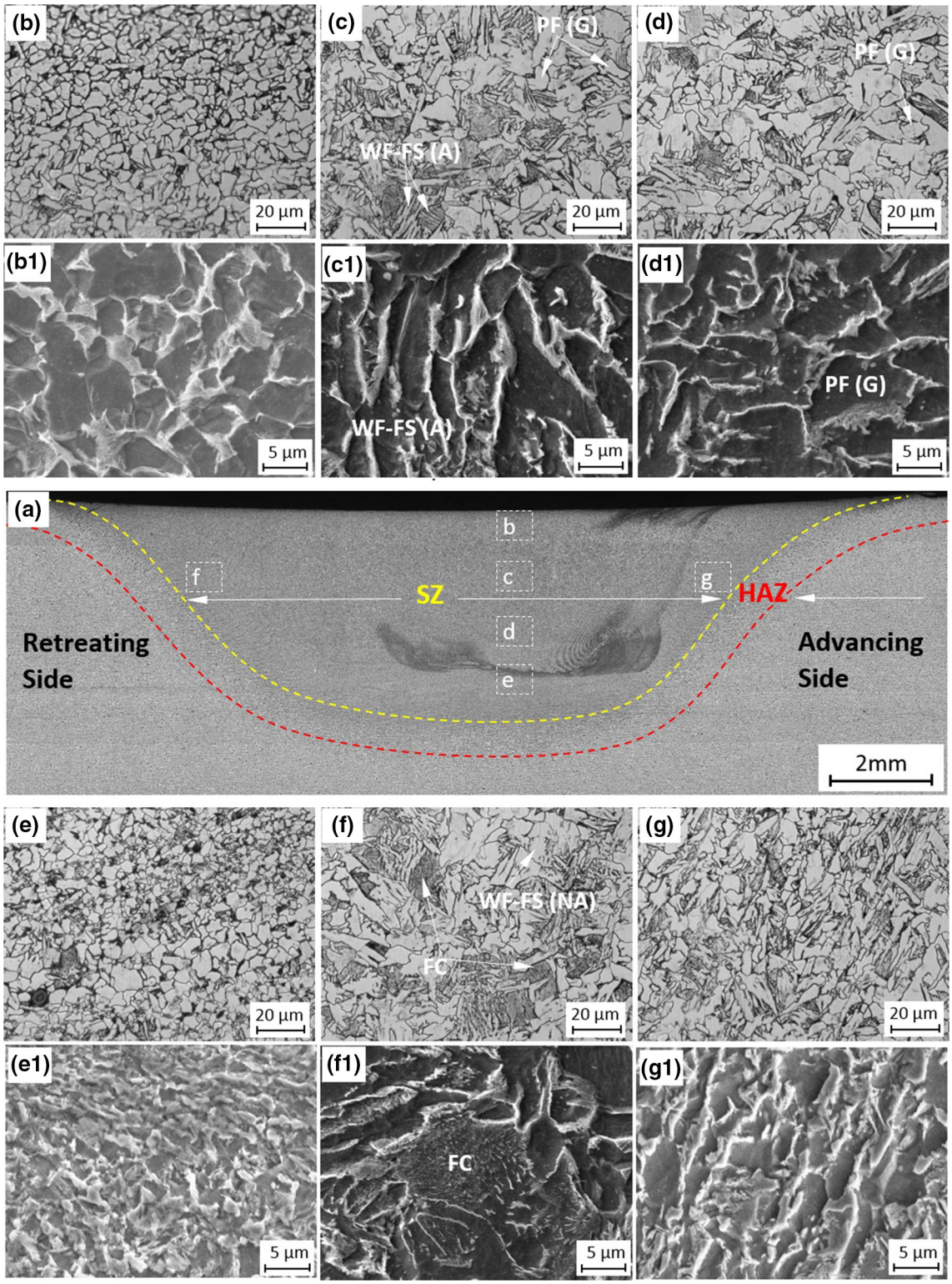

Fig. 3—Optical and SEM micrographs showing the global and detailed microstructures of FSPed Grade A steel sample: (*a*) A general view of cross section of the sample perpendicular to the advancing direction, (*b*)-(*b1*) the shoulder-effected SZ, (*c*)-(*c1*)-(*d*)-(*d1*) the SZ from top of the surface through the subsurface, (*e*)-(*e1*) edge of the pin-effected SZ, (*f*, *f1*) transition region on retreating side, and (*g*)-(*g1*) transition region on advancing side.

with the sizes in the range of 0.5 to 10 μm along with fine perlite grains. Ferrite laths start growing preferably along austenite grain boundaries, and they seem to be islands of micro-phase in the ferrite matrix within the prior austenite grains depending on the observation plane; the micro-phases may appear non-aligned as in

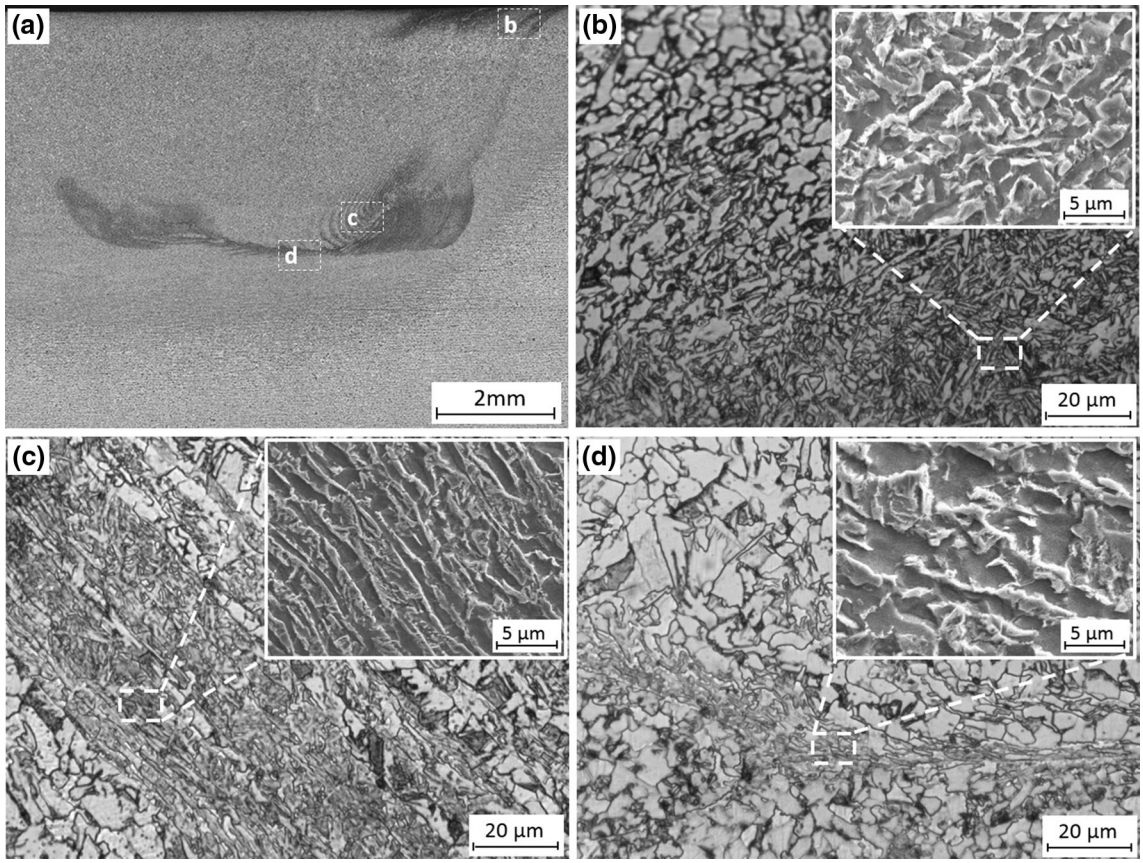

Fig. 4—Optical and SEM micrographs showing the detailed microstructures around the pin in the stir zone: (*a*) A general view of the SZ, (*b*) UFG structure in the upper side of the pin through the advancing side, (*c*) onion ring structure formed along the pin edge, and (*d*) structure showing the flow lines beneath the pin tip.

the case of Figure 3(f). At high transformation temperatures, pearlite is generally observed as nodules of alternate ferrite and cementite lamellae that may be quite coarse and degenerate. The lamella of microstructure in the SZ appears as a ferrite—cementite aggregate (Figure 3(f1)). In that region, the cementite lamella degenerates inside the pearlite phase due to high transformation temperature, and the ferrite phase transforms into a nodular structure. In the SZ, this structure appears as the cluster of ferrite–cementite (FC) as shown in Figure 3(f). The microstructure of SZ is not only the result of a purely displacive transformation but is also formed by deformation direction as in the case of the zone in Figure 3(g). The microstructure in that zone consists mainly of the elongated ribbon-shaped grains.

Material flow plays a dominant role in forming the microstructure of the processed zone during FSP. Material flow generally occurs through the retreating side (RS) of the SZ, and the plasticized material transports behind the tool from the advancing side to the retreating side. As known, the centers of rotating pins and stir zone are not in the same alignment, and the SZ is formed in an asymmetric geometry as seen in Figure 3(a)). As a result of that misalignment, the material flow is very complex around the tool.[40] Thus, a detailed microstructural investigation was also undertaken around the pin, and some representative micrographs showing the detailed microstructure as well as flowing regions are shown in Figure 4.

In the vortex-like shaped processed zone, no tunneling cavity and slot formations appear behind the pin in the SZ. However, the pin behaves like a severe forging around itself. The results reveal that the main parts of the material flow occur near the top surface and at the retreating side. Material near the top surface was stretched to the advancing side resulting in a non-symmetrical shape of the stir zone[40] (Figure 4(b)). The bottom and top of advancing sides of the tool pin was subjected to an extreme plastic deformation. As a result, UFG microstructure is formed around the pin due to the effects of dynamic recrystallization and rapid cooling. Tutunchilar *et al.*[41] simulated the material flow during FSP by DEFORM 3D software. Their experimental and numerical results showed that the formation of material flow pattern occurred near the top surface of the sample at the advancing side as in the case of the current study (Figure 4(b)). On the other hand, a unique region called "onion ring structure" was also observed within the SZ as shown in Figure 4(c). That region has relatively oriented microstructure with fine grains having flow patterns like onion rings. Such microstructural formation was attributed to the characteristic movement

of the material[42,43] and to the precipitations in the onion ring structure and / or to a sudden change in the grain size of that region.[44,45]

Detailed images showing the characteristics of material flow lines just under the pin are shown in Figure 4(d). The material flow lines inside that region are mainly similar to those inside the regions just under the shoulder and inside the region of onion rings.[40] The darker lines or regions are due to the influence of etching of UFG microstructure formed around the pin. Such microstructural formations might be formed by relatively high cooling rate and adequate dynamic recrystallization during FSP. It is known that increasing deformation rate near the surface or around the pins gives rise to a special microstructure having generally UFG structure.[46] A numerical study was done by Cho *et al.*[47] on that phenomenon, and they reported an intense deformation around the pin where UFG microstructure was formed.

TEM micrographs taken from the region in Figure 3(b) are shown in Figure 5 to show the sub-micron-sized micro-constitutions in the SZ. Fine microstructure including relatively coarse martensite phase is evident in that zone (Figure 5(a)). The coarse martensite units formed in the shape of laths are composed of high density of dislocations (Figure 5(a)). This formation suggests that the initial microstructure (ferrite + pearlite) transforms into martensitic phase with high dislocation density due to intense plastic deformation and rapid cooling during FSP.[2] Figure 5(b) shows TEM micrograph of the Widmanstatten ferrite with low dislocation density in the SZ. Widmanstatten ferrite that grows at prior austenite grain boundaries is usually formed as colonies of coarse side plates with aligned microstructure (Figure 5(b)). Individual plates are separated by low angle grain boundaries as clearly distinguished in TEM image given in Figure 5(b).[39] Shear bands comprising highly misoriented fine sub-grains are also observed, and they align approximately perpendicular to Widmanstatten plates.[48] The TEM micrograph in Figure 5(c) represents the ferrite–cementite (FC) aggregates. They consist of a ferritic matrix interspersed with irregular-shaped particles and elongated fibers. The dimension of fibers is in the range between 250 and 1500 nm. The dimensions of irregular-shaped particles are in the range of 50 to 500 nm. Formation of the FC aggregate starts just before or after the starting of growth of the Widmanstatten ferrite. However, it completes just before or after the starting of the bainitic transformation.[49] Di Martino *et al.*[49] reported a transformation sequence of phases as follows: Primary Ferrite, Pearlite, Widmanstatten Ferrite, Ferrite Cementite Aggregate, Bainite, and Martensite.[49]

A typical sub-grain structure is also formed during FSP in the SZ as shown in Figure 5(d). The sub-grains have the shape of walls made of parallel dislocations and networks of dislocations with hexagonal shape. It is clearly seen that the dislocation density is relatively low inside the sub-grains, and most of them are accumulated and tangled with others around the sub-grain boundaries.

A transition region (zone) which is not exposed to deformation (a micro-scale deformation may well be formed) is formed during FSP. This zone is similar to the HAZ formed in fusion-based welding processes.[50] So further investigation is needed for clarifying the microstructural changes through that zone. Therefore, a systematic study was made at various points of the HAZ with the aid of the section of the Fe-Fe3C phase diagram as shown in Figure 6. The HAZ can be separated into three sub-regions depending on the peak temperature (Figure 6(a)). They can be named as *"fine-grained HAZ,"* *"inter-critical HAZ,"* and *"sub-critical HAZ"* as in the case of fusion welding of steels.[50,51] However, no *"coarse-grained HAZ"* is observed in the present study on the contrary to that of fusion welding of steels. The highest temperature is about 1103 K (930 °C) in the SZ which is lower than the temperature that may cause grain coarsening. The peak temperature defines the size of each region. The vertical line in the phase diagram indicates the composition of the current grade A steel. These intercepts were then projected horizontally until they intersect the temperature gradient curve (Figure 6(a)). This second intercept is then extended vertically and downward to the processed zone to reveal the relative width of each HAZ region.

The microstructure of unaffected zone is the same with the base material (Figure 6(b)). The *"sub-critical HAZ"* is between the *inter-critical HAZ* and unaffected base steel, and it is subjected to the peak temperatures below the *A1*. At temperatures just below the *A1*, carbide plates into the pearlitic region begin spheroidizing. A representative microstructure of sub-critical HAZ consisting of spheroidized carbide and ferrite grains is shown in Figure 6(c). It can be said that a tempering heat treatment takes place in that region. However, the pearlite does not completely spheroidize, because the thermal cycle is too short for spheroidization to take place. However, microstructural observations imply that the material in the region of spheroidized carbides experiences sufficient time below the *A1* temperature to allow partial homogenization and spheroidization of the cementite.[46] The inter-critical heat-affected zone (ICHAZ) is adjacent to the *"fine-grained HAZ"* which is subjected to the peak temperatures between *Ac3* and *A1,* where the ferrites and carbides of base steel start transforming into austenite. A bimodal microstructure having both fine and relatively coarse-grained ferrites is formed in that region (Figure 6(d)). It can be said that a normalization heat treatment of the base steel occurs in that region. The thermal cycle causes transformation of the pearlite to austenite on heating (with the reverse reaction on cooling) and results in refinement of the pearlite colonies and some of the ferrite grains.[52] The microstructural results also indicate that the partial grain refinement in the ICHAZ increases with the effective peak temperatures from *A1* to *A3*. Representative micrographs showing this formation in the ICHAZ are shown in Figure 6(d).[51] The *"fine-grained (FG) HAZ"* is adjacent to the *"coarse-grained (CG) HAZ."* The steel in that zone is subjected to the peak temperatures below the recrystallization temperature but above the *Ac3* (the equilibrium cooling temperature

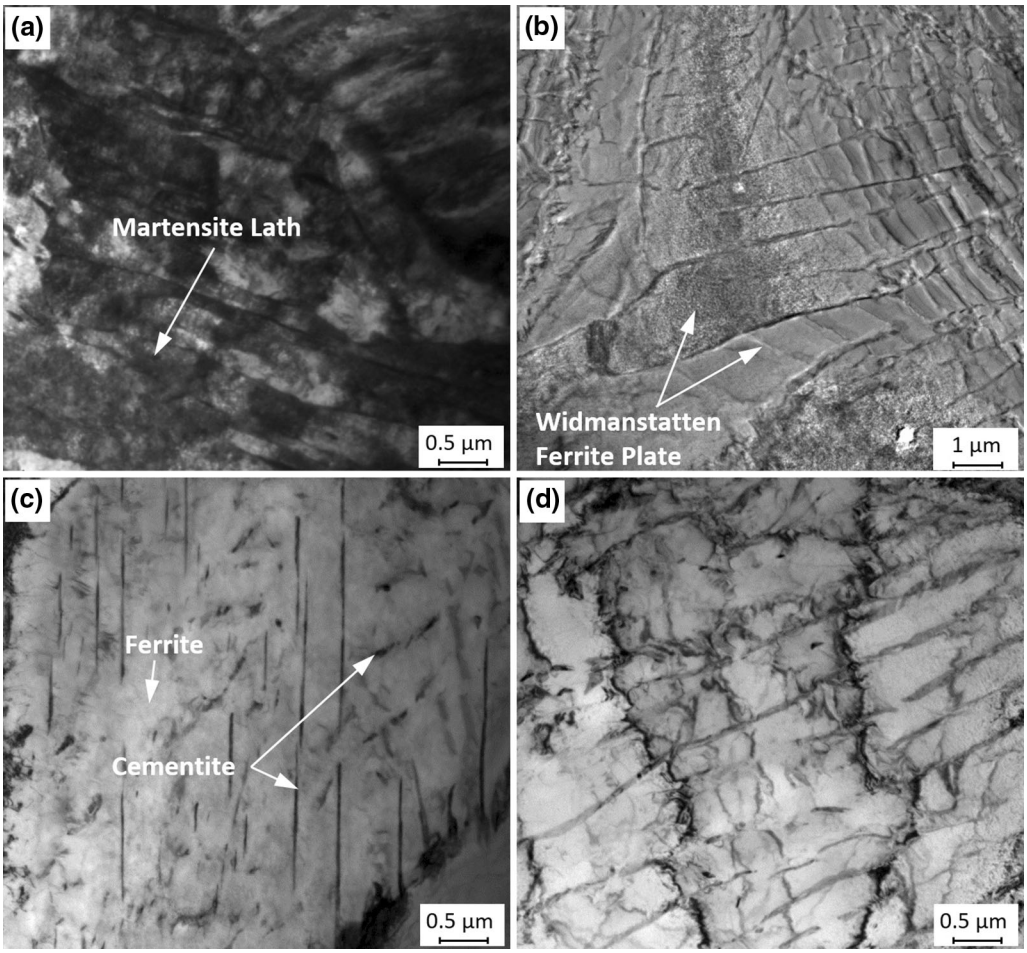

Fig. 5—TEM bright field micrographs taken from stir zone showing: (*a*) martensite laths, (*b*) Widmanstatten ferrite, (*c*) ferrite–cementite aggregates (FC), and (*d*) ferritic microstructure consisting of sub-grains formed by polygonization of dislocations.

at which some of the austenite transforms to ferrite). A representative micrograph of the FGHAZ consisting of small ferritic grains and pearlite is shown in Figure 6(e). Since the peak temperature is below the recrystallization temperature, abnormal or rapid grain growth of austenite phase does not occur in that zone. Moreover, inclusions at the grain boundaries help in preventing the grain boundary sliding, and hence grain growth is very limited although relatively high peak temperatures are reached.[53–56] Microstructural results indicate that the peak temperatures encountered in the refined region fell just above the effective *A3* temperature. The decomposition of austenite to ferrite and pearlite on cooling stage promotes more refinement in the microstructure in that region.

B. *Hardness and Tensile Test Results*

The hardness profile taken from the vertical cross section of FSPed samples is shown in Figure 7(a). As shown, the hardness of steel increased from 140 Hv0.3 to about 200 Hv0.3 in the SZ after FSP due to the substantial grain refinement and increase in dislocation density.[57] However, the surface layer just beneath the shoulder has relatively low hardness of about 195 Hv0.3. This may be due to the effect of early recrystallization and grain coarsening coming from relatively high pressing effect of the shoulder.[58] Ultrafine-grained microstructure formed around and under the pin increased the hardness of base steel substantially to about 245 Hv0.3 due to the pin's forging effect and intense deformation as a result of the rotation of the pin. After the peak value around the pin end, the hardness starts decreasing through the rest of the sample. However, hardness values measured in the HAZ of the FSPed steel are still higher than those of the base material (Figure 7(b)), because a temperature-induced structural alteration without intense deformation takes place in that zone. The hardness value, however, continues to decrease and reaches a stable level near the other surface of the plate with the hardness values higher than that of the base material. Considering the sheet thickness of 6 mm and total processed zone depth of 3.5 mm, this result is normal. The heat generated by FSP affects the microstructure down to the other surface of the plate.

To show the homogeneity of hardness distribution throughout the processed zone, systematic micro-hardness measurements were carried out, and the results were plotted as a contour map in Figure 7(c). This map

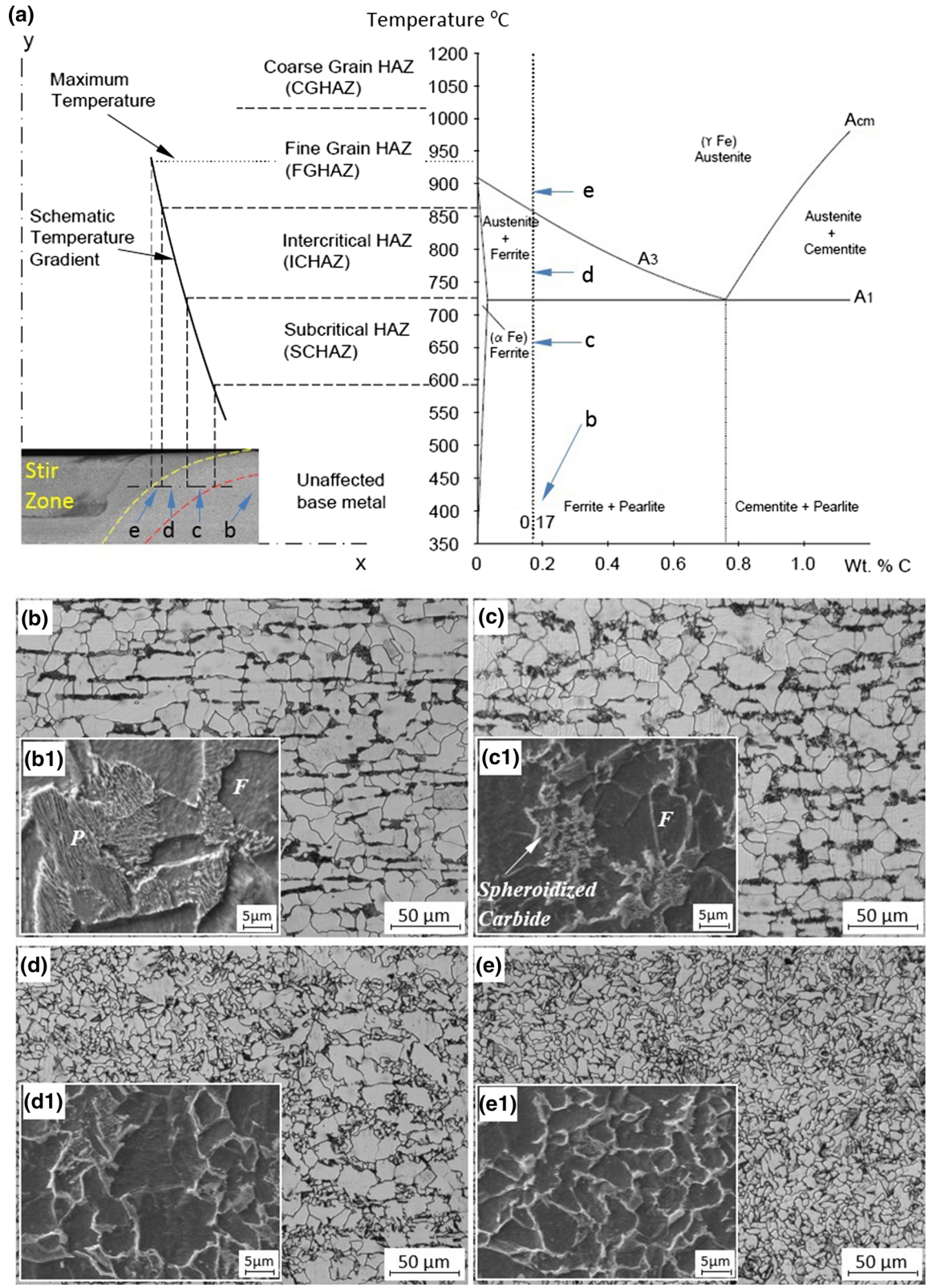

Fig. 6—Microstructural evolution in various points of the HAZ of FSPed steel: (*a*) A section of the Fe-Fe3C phase diagram and the sub-sections of HAZs. Optical micrographs and SEM micrographs (inside the optical micrographs) showing the microstructures of (*b*) unaffected base steel, (*c*) SCHAZ, (*d*) ICHAZ, and (*e*) FGHAZ.

corresponds well with the micrographs showing the global microstructural alteration in Figures 7(a) and (b). Microstructural inhomogeneity especially in the SZ brought about a considerable variation in the hardness values throughout that zone. As clearly seen, the regions having more refined microstructure also have higher hardness values compared to the regions having coarser grains in that map. As pointed out in Figure 8, the bottom and top of advancing sides of the tool pin subjected to severe plastic deformation resulted in a UFG microstructure. This substantial grain refinement also brought about a considerable increase in hardness compared to other processed zones having fine-grained structure. This variation in hardness values is in good agreement with the results of line scan hardness measurements given in Figures 7(a) and (b).

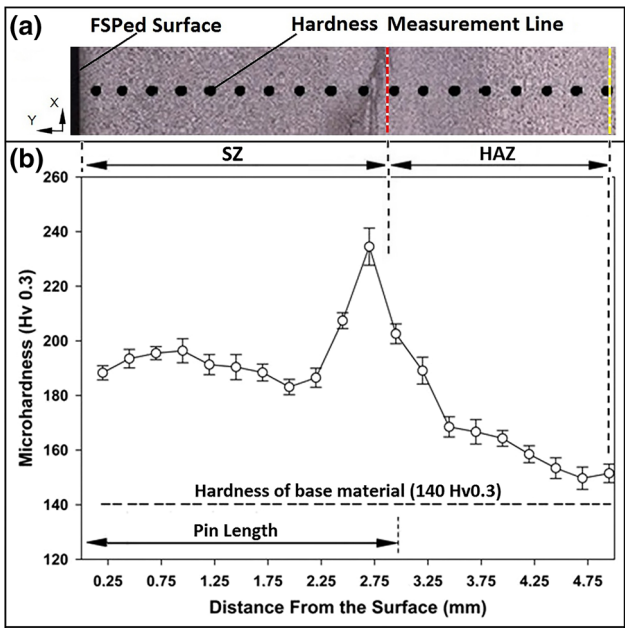

Fig. 7—(*a*) Optical micrograph showing the cross section of the processed zone where the hardness measurements were taken and (*b*) hardness profiles showing the hardness variations along the distance from the surface of FSPed sample.

The strength and ductility values of steel before and after FSP are summarized in Table I. FSP leads to a remarkable increase in strength values without considerably sacrificing the ductility as compared to the initial CG material. Both yield and tensile strength values increased from 256 and 435 MPa to about 334 and 525 MPa, respectively. Such improvement in the strength of FSPed steel is primarily because of the considerably refined microstructure leading to fine grain strengthening.[32] In the processed microstructure, the refined grains are separated mostly by high angle of boundaries. However, as given in Figure 5(b), the sub-grains separated by low angle boundaries are also formed especially inside the ferritic grains. Hence, LAGBs may also contribute to the increase in strength after FSP.[26] On the other hand, it is well known that dislocation density increases during FSP, and this formation makes a further effect on the strengthening of the FSPed microstructure.[58] The formation of dislocations is clearly seen in TEM micrographs (Figure 5). More importantly, the strengthening during FSP is achieved without a considerable decline of ductility, which is a crucial parameter considering the engineering applications of the steels. In CG state, the uniform and failure

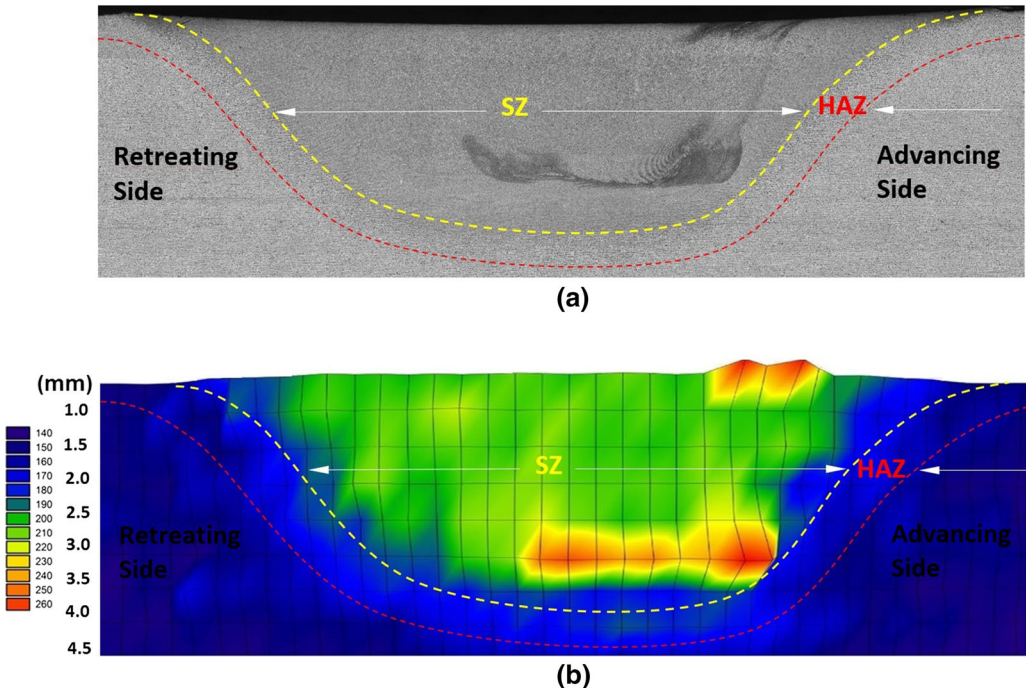

Fig. 8—(*a*) Optical microstructure of cross section of the FSPed sample perpendicular to the advancing direction and (*b*) a contour map showing the distribution of hardness values throughout the FSPed zone.

Table I. Main Strength and Ductility Values of Grade A Steel Before and After FSP

Condition	Yield Strength (MPa)	Tensile Strength (MPa)	Uniform Elongation (Pct)	Failure Elongation (Pct)
base	256 ± 07	435 ± 06	18.4 ± 0.3	44.2 ± 2.4
FSPed	334 ± 06	525 ± 13	13.9 ± 0.6	32.4 ± 1.7

elongation values are 18.4 and 44.2 pct, respectively. After FSP, the failure elongation value decreases to about 32.4 pct. Also a uniform elongation of about 13.9 pct is still retained after FSP. A moderate decrease in ductility is related to the decrease in strain hardening capacity of the FG steel after FSP. Lower strain hardenability of the FSPed steel may be related to its refined grain size and increased dislocation density. Interactions of the dislocation with each other or other microstructural obstacles like HAGBs are the main hardening mechanism. Dislocation free path decreases with deceasing HAGB spacing. Thus, dislocation accumulation to initiate a micro-crack requires lower plastic deformation due to higher number of grains contributing to this process. Hence macroscopic necking starts relatively easily at smaller plastic strains which leads to a lower uniform elongation.

IV. CONCLUSIONS

A low carbon steel (Grade A) used mainly for ship construction was processed by single-pass FSP at room temperature, and the alterations in its microstructure as well as hardness and tensile properties were investigated. The main results and conclusions of this study can be summarized as follows:

1. FSP decreases the ferritic grain size of Grade A steel from 25 μm in the coarse-grained state to about 3 μm in the fine-grained state, and the fine grains are separated mostly by high angle of boundaries with low density of dislocations. The processed zone also has inhomogeneity regarding the microstructure. Some regions with ultrafine-grained (UFG) microstructure are formed especially around the pin due to the dynamic recrystallization and rapid cooling effects.
2. Two main distinct regions called stir zone (SZ) and heat-effected zone (HAZ) are formed by single-pass FSP of the steel plate. The SZ and HAZ consist mainly of ferrite, widmanstatten ferrite, ferrite + cementite aggregates, and martensite.
3. HAZ formed during FSP is separated into three sub-regions named as "fine-grained HAZ," "inter-critical HAZ," and "sub-critical HAZ" depending on the peak temperature as in the case of fusion welding of steels. No "coarse-grained HAZ" is observed in the current study on the contrary to fusion welding of steels.
4. The hardness of the steel plate increased from 140 Hv0.3 to about 200 Hv0.3 in the SZ, and ultrafine-grained microstructure formed around the pin during FSP increased the hardness to about 245 Hv0.3.
5. FSP leads to a remarkable increase in strength values without considerably sacrificing the ductility as compared to the initial CG material. Both yield and tensile strength values increased from 256 and 435 MPa to about 334 and 525 MPa, respectively. The uniform and failure elongation values of 18.4 and 44.2 pct for CG steel decreased to about 13.9 and 32.4 pct, respectively.

ACKNOWLEDGMENTS

Dr. G. Purcek was supported by The World Academy of Sciences (TWAS) under the Visiting Researchers Program of TWAS-UNESCO Associateship Scheme (Ref. 3240260896). The authors would like to thank Dr. T. Kucukomeroglu for his help in conducting the FSP.

REFERENCES

1. A. Ozekcin, H.W. Jin, J.Y. Koo, N.V. Bangaru, R. Ayer, and G. Vaughn: *Int. J. Offshore Polar Eng.*, 2004, vol. 14, pp. 1053–5381.
2. P. Xue, B.L. Xiao, W.G. Wang, Q. Zhang, D. Wang, Q.Z. Wang *et al.*: *Mater. Sci. Eng. A.*, 2013, vol. 575, pp. 30–34.
3. G. Purcek, O. Saray, I. Karaman, and T. Kucukomeroglu: *Mater. Sci. Eng. A.*, 2008, vol. 490, pp. 403–10.
4. A. Azushima, R. Kopp, A. Korhonen, D.Y. Yang, F. Micari, G.D. Lahoti *et al.*: *CIRP Ann. Manuf. Technol.*, 2008, vol. 57, pp. 716–35.
5. R.Z. Valiev and T.G. Langdon: *Prog. Mater. Sci.*, 2006, vol. 51, pp. 881–981.
6. S.M. Aktarer, D.M. Sekban, O. Saray, T. Kucukomeroglu, Z.Y. Ma, and G. Purcek: *Mater. Sci. Eng. A.*, 2015, vol. 636, pp. 311–19.
7. Z.Y. Ma: *Metall. Mater. Trans. A.*, 2008, vol. 39, pp. 642–58.
8. R.S. Mishra and Z.Y. Ma: *Mater. Sci. Eng. R Reports.*, 2005, vol. 50, pp. 1–78.
9. Y.N. Zhang, X. Cao, S. Larose, and P. Wanjara: *Can. Metall. Q.*, 2012, vol. 51, pp. 250–61.
10. H.S. Arora, H. Singh, and B.K. Dhindaw: *Int. J. Adv. Manuf. Technol.*, 2012, vol. 61, pp. 1043–55.
11. R.S. Mishra and Z.Y. Ma: *Mater. Sci. Eng. R Reports.*, 2005, vol. 50, pp. 1–78.
12. Y.C. Chen and K. Nakata: *Mater. Charact.*, 2009, vol. 60, pp. 1471–75.
13. D.M. Sekban, O. Saray, S.M. Aktarer, G. Purcek, and Z.Y. Ma: *Mater. Sci. Eng. A.*, 2015, vol. 642, pp. 57–64.
14. A. Chabok and K. Dehghani: *Mater. Sci. Eng. A.*, 2010, vol. 528, pp. 309–13.
15. C. Lorenzo-Martin and O.O. Ajayi: *Wear*, 2015, vols. 332–333, pp. 962–70.
16. S.H. Aldajah, O.O. Ajayi, G.R. Fenske, and S. David: *Wear*, 2009, vol. 267, pp. 350–55.
17. A. Rahbar-kelishami, A. Abdollah-zadeh, M.M. Hadavi, R.A. Seraj, and A.P. Gerlich: *Appl. Surf. Sci.*, 2014, vol. 316, pp. 501–07.
18. M.I. Costa, D. Verdera, M.T. Vieira, and D.M. Rodrigues: *Appl. Surf. Sci.*, 2014, vol. 296, pp. 214–20.
19. S. Khodir, Y. Morisada, and H. Fujii: *J. Mater. Sci.*, 2013, vol. 48, pp. 4313–20.

20. P. Xue, Z.Y. Ma, Y. Komizo, and H. Fujii: *Mater. Lett.*, 2016, vol. 162, pp. 161–64.
21. M. Abbasi, T.W. Nelson, and C.D. Sorensen: *Metall. Mater. Trans. A*, 2012, vol. 43, pp. 4940–46.
22. N. Yasavol and H. Jafari: *J. Mater. Eng. Perform.*, 2015, vol. 24, pp. 2151–57.
23. N. Yasavol, A. Abdollah-Zadeh, M.T. Vieira, and H.R. Jafarian: *Appl. Surf. Sci.*, 2014, vol. 293, pp. 151–59.
24. Y. Morisada, H. Fujii, T. Mizuno, G. Abe, T. Nagaoka, and M. Fukusumi: *Surf. Coatings Technol.*, 2011, vol. 205, pp. 3397–3403.
25. M.H. Razmpoosh, A. Zarei-Hanzaki, and A. Imandoust: *Mater. Sci. Eng. A.*, 2015, vol. 638, pp. 15–19.
26. M.I. Costa, C. Leitão, A. Ramalho, and D.M. Rodrigues: *J. Mater. Process. Technol.*, 2015, vol. 217, pp. 272–77.
27. A. Amirafshar and H. Pouraliakbar: *Meas. J. Int. Meas. Confed.*, 2015, vol. 68, pp. 111–16.
28. R. Li, T. Yuan, Z. Qiu, K. Zhou, and J. Li: *Surf. Coat. Technol.*, 2014, vol. 258, pp. 415–25.
29. H.S. Grewal, H.S. Arora, H. Singh, A. Agrawal, and S. Mukherjee: *J. Tribol.*, 2014, vol. 136, pp. 1–10.
30. H.S. Grewal, H.S. Arora, H. Singh, and A. Agrawal: *Appl. Surf. Sci.*, 2013, vol. 268, pp. 547–55.
31. S. Noh, R. Kasada, A. Kimura, S.H.C. Park, and S. Hirano: *J. Nucl. Mater.*, 2011, vol. 417, pp. 245–48.
32. M. Hajian, A. Abdollah-zadeh, S.S. Rezaei-Nejad, H. Assadi, S.M.M. Hadavi, K. Chung *et al.*: *Mater. Des.*, 2015, vol. 67, pp. 82–94.
33. J.D. Escobar, E. Velásquez, T.F.A. Santos, A.J. Ramirez, and D. López: *Wear.*, 2013, vol. 297, pp. 998–1005.
34. S. Dodds, A.H. Jones, and S. Cater: *Wear.*, 2013, vol. 302, pp. 863–77.
35. M. Mehranfar and K. Dehghani: *Mater. Sci. Eng. A.*, 2011, vol. 528, pp. 3404–08.
36. Y.S. Sato, T.W. Nelson, and C.J. Sterling: *Acta Mater.*, 2005, vol. 53, pp. 637–45.
37. International Institute for Welding Document IX-1533-88 IXJ-123-87 Revision 2, *Guide to the Light Microscope Examination of Ferritic Steel Weld Metals.*, 1998.
38. M. Jafarzadegan, A.H. Feng, A. Abdollah-Zadeh, T. Saeid, J. Shen, and H. Assadi: *Mater. Charact.*, 2012, vol. 74, pp. 28–41.
39. G. Thewlis: *Mater. Sci. Technol.*, 2004, vol. 20, pp. 143–60.
40. X. He, F. Gu, and A. Ball: *Prog. Mater. Sci.*, 2014, vol. 65, pp. 1–66.
41. S. Tutunchilar, M. Haghpanahi, M.K.B. Givi, P. Asadi, and P. Bahemmat: *Mater. Des.*, 2012, vol. 40, pp. 415–26.
42. K.N. Krishnan: *Mater. Sci. Eng. A.*, 2002, vol. 327, pp. 246–51.
43. K. Kumar and S.V. Kailas: *Mater. Sci. Eng. A.*, 2008, vol. 485, pp. 367–74.
44. M.W. Mahoney, C.G. Rhodes, J.G. Flintoff, W.H. Bingel, and R.A. Spurling: *Metall. Mater. Trans. A.*, 1998, vol. 29, pp. 1955–64.
45. M.A. Sutton, B. Yang, A.P. Reynolds, and R. Taylor: *Mater. Sci. Eng. A.*, 2002, vol. 323, pp. 160–66.
46. T. Lienert and W.S. Jr: *Weld. J. Res. Suppl.*, 2003, vol. 82, pp. 1–9.
47. J.-H. Cho, D.E. Boyce, and P.R. Dawson: *Mater. Sci. Eng. A.*, 2005, vol. 398, pp. 146–63.
48. P. Cizek, F. Bai, W.M. Rainforth, and J.H. Beynon: *Mater. Trans.*, 2004, vol. 45, pp. 2157–64.
49. S.F. Di Martino and G. Thewlis: *Metall. Mater. Trans. A.*, 2014, vol. 45, pp. 579–94.
50. P.L. Threadgill: *Sci. Technol. Weld. Join.*, 2007, vol. 12, pp. 357–60.
51. J.C. Lippold: *Welding Metallurgy and Weldability*, Wiley, Hoboken, 2014.
52. J. Benjamin: *Sci. Am.*, 1976, vol. 234 (5), pp. 40–48.
53. B. Burton: *Philos. Mag. A.*, 2002, vol. 82, pp. 2303–20.
54. I. Milas and E.A. Carter: *J. Mater. Sci.*, 2009, vol. 44, p. 1741.
55. C.B. Smith, W. Crusan, J.R. Hootman, J.F. Hinrichs, R.J. Heideman and J.S. Noruk: *2001 TMS Annu. Meet. Automot. Alloy. Join. Alum. Symp. (Aluminum 2001),* 2001, pp. 175–185.
56. Y. Sugino, S. Ukai, B. Leng, N. Oono, S. Hayashi, T. Kaito *et al.*: *J. Nucl. Mater.*, 2014, vol. 452, pp. 628–32.
57. J.-Q. Su, T.W. Nelson, and C.J. Sterling: *Mater. Sci. Eng. A.*, 2005, vol. 405, pp. 277–86.
58. P.B. Prangnell and C.P. Heason: *Acta Mater.*, 2005, vol. 53, pp. 3179–92.